

Buckling in serpentine microstructures and applications in elastomer-supported ultra-stretchable electronics with high areal coverage†

Cite this: *Soft Matter*, 2013, 9, 8062

Yihui Zhang,^{†ab} Sheng Xu,^{†c} Haoran Fu,^{ad} Juhwan Lee,^c Jessica Su,^c Keh-Chih Hwang,^{be} John A. Rogers^{*c} and Yonggang Huang^{*afg}

Lithographically defined electrical interconnects with thin, filamentary serpentine layouts have been widely explored for use in stretchable electronics supported by elastomeric substrates. We present a systematic and thorough study of buckling physics in such stretchable serpentine microstructures, and a strategic design of the serpentine layout for an ultra-stretchable electrode, *via* analytical models, finite element method (FEM) computations, and quantitative experiments. Both the onset of buckling and the postbuckling behaviors are examined, to determine scaling laws for the critical buckling strain and the limits of elastic behavior. Two buckling modes, namely the symmetric and anti-symmetric modes, are identified and analyzed, with experimental images and numerical results that show remarkable levels of agreement for the associated postbuckling processes. Based on these studies and an optimization of the design layout, we demonstrate routes for application of serpentine interconnects in an ultra-stretchable electrode that offer, simultaneously, an areal coverage as high as 81% and a biaxial stretchability as large as ~170%.

Received 14th May 2013

Accepted 26th June 2013

DOI: 10.1039/c3sm51360b

www.rsc.org/softmatter

1 Introduction

Elastically stretchable electronics based on elastomeric substrates could bridge the gap between traditional rigid electronic devices and soft curvilinear environment. These devices and systems are of increasing interest^{1–12} due to their ability to provide applications that cannot be addressed with established technologies, ranging from wearable photovoltaics¹³ to 'epidermal' health/wellness monitors,¹⁴ to curvilinear digital cameras,^{15,16} to bio-integrated therapeutic devices^{17,18} and sensitive robotic skins.^{19–22} When implemented with advanced materials and mechanics designs, such devices can be deformed like a rubber band, twisted like a rope, and bent

around the tip of a pencil, without mechanical fatigue or any significant change in operating characteristics, even when brittle materials are used.^{7,23–25} Many of these systems exploit island-bridge architectures, in which the active components reside at the islands and electrical interconnects form the bridges; the latter are largely responsible for the stretchability. Generally, stretchable devices must accommodate two competing design goals: (1) achieving a high surface filling ratio, which requires high coverage of the islands, and (2) affording high mechanical stretchability, which typically demands long bridges between these islands. At least two classes of bridge structures have been proposed: (i) straight ribbons in arc-shaped layouts that result from Euler buckling^{15,16,26} and (ii) serpentine traces that also involve non-coplanar geometries, in either or both the as-fabricated and as-deformed states.^{14,27–31} The first involves a comparatively simple geometry, with deformation mechanisms that have been thoroughly investigated extensively *via* experiments and fundamental mechanics theory.^{32–34} The serpentine interconnect represents an advanced embodiment, with improved stretchability for a given spacing between adjacent islands. When fabricated in an ultra-thin form and mounted on a thin elastomeric substrate (*e.g.*, polydimethylsiloxane and ecoflex), the serpentine interconnect could be conformably mounted on the human skin,¹⁴ because of its ultra-soft feature (with the effective modulus as low as that (~100 kPa) of the human skin). The complex geometries and complicated buckling mechanisms, however, render their study suitable only through numerical simulations for some specific geometric parameters.²⁹ Partly as

^aDepartment of Civil and Environmental Engineering and Department of Mechanical Engineering, Northwestern University, Evanston, IL 60208, USA. E-mail: y-huang@northwestern.edu

^bCenter for Mechanics and Materials, Tsinghua University, Beijing 100084, China

^cDepartment of Materials Science and Engineering, Frederick Seitz Materials Research Laboratory, University of Illinois at Urbana-Champaign, Urbana, Illinois 61801, USA. E-mail: jrogers@illinois.edu

^dDepartment of Civil Engineering, Zhejiang University, Hangzhou, 310058, China

^eAML, Department of Engineering Mechanics, Tsinghua University, Beijing 100084, China

^fInstitute of Public Health and Medicine, Northwestern University, Evanston, IL 60208, USA

^gSkin Disease Research Center, Feinberg School of Medicine, Northwestern University, Evanston, IL 60208, USA

† Electronic supplementary information (ESI) available. See DOI: 10.1039/c3sm51360b

‡ These authors contributed equally to this work.

as a result, the general, underlying mechanics that govern the critical buckling and postbuckling processes remain unclear, and scaling laws have not been reported previously.

The motivation of this study is to present a systematic investigation of the onset of buckling and postbuckling behavior in serpentine interconnects, and to demonstrate a strategic design of an electrode with both high stretchability and areal coverage, through combined analytical modeling, numerical simulations, and experimental observations. Here, we focus on the serpentine interconnects that are not bonded to the elastomeric substrate such that they could deform freely and the interconnect–substrate interaction could be neglected. Such a type of serpentine interconnect could be realized in fabrication through two approaches: (i) adopting the molded relief structure on the elastomeric substrate,^{26,35} and bonding the islands onto the top of the raised relief, as shown in Fig. 1a; (ii) using a flat substrate, and selectively bonding the islands onto the substrate,^{29,36} while leaving the serpentine interconnect with a weak interaction with the substrate. For some applications,^{14,30,37–39} the serpentine interconnects could be either bonded to or embedded in the substrate such that the substrate would exert a strong constraint on the deformation of serpentine interconnects, which is beyond the scope of the present study. For free-standing serpentine interconnects adopted in

stretchable electronics, they usually have much smaller thicknesses (*e.g.*, several hundreds of nanometers) than their widths (*e.g.*, several tens of microns),^{14,27,29} so as to offer a high flexibility. When stretching such serpentine interconnects, the in-plane bending deformation would induce a relatively large strain energy, and thus buckling would occur to trigger out-of-plane bending and twisting, *i.e.*, the so-called lateral buckling,⁴⁰ so as to reduce the strain energy. Our theoretical and numerical analyses show two different buckling modes and the associated postbuckling processes, which are validated by experiments. The correlations between the stretchability and various geometric parameters are established, as design guidelines for practical applications. Furthermore, we demonstrate an optimized serpentine interconnect as part of an ultra-stretchable metal electrode that offers both high areal coverage of islands and large stretchability at the system level, thereby outperforming examples reported previously.

2 Experimental section

On a silicon wafer, sequential spin coating defined a bilayer of poly(methyl methacrylate) (Microchem, PMMA 495 A2, 3000 rpm for 30 s, baked on a hotplate at 180 °C for 2 min) and polyimide (Sigma Aldrich, PI, from poly(pyromellitic

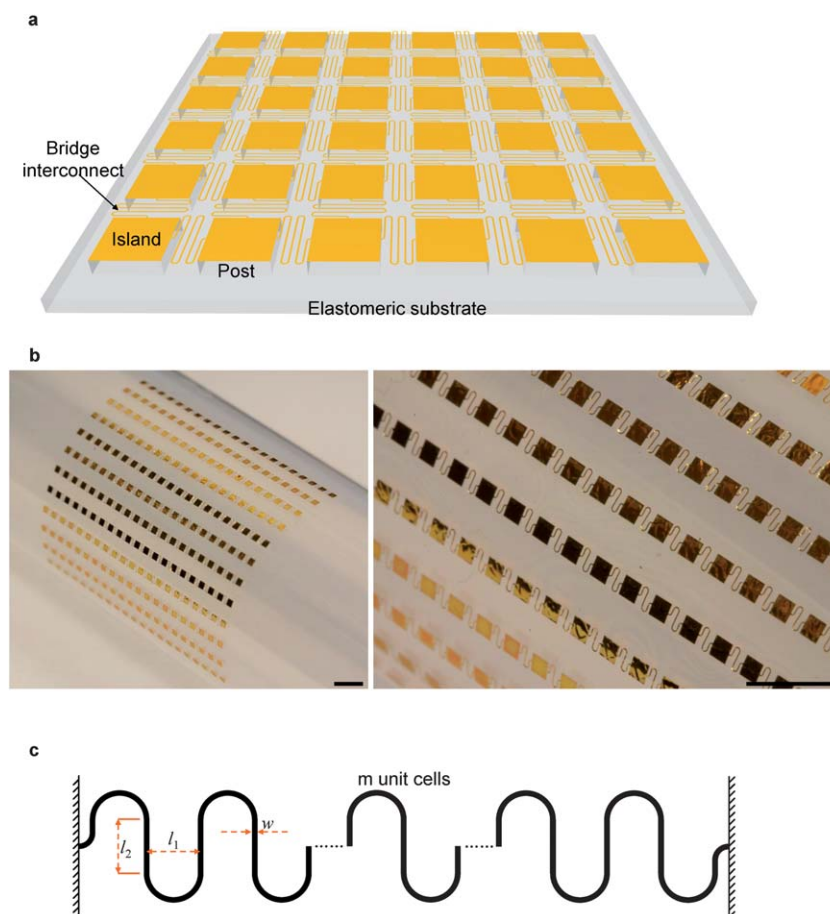


Fig. 1 (a) Schematic of the island-bridge structure with serpentine geometry; (b) optical image of the as-fabricated serpentine structures; (c) illustration of geometric parameters for a serpentine interconnect with m unit cells. The scale bars in (b) are 5 mm.

dianhydride-co-4,4'-oxydianiline)amic acid solution; 4000 rpm for 30 s, baked on a hotplate at 150 °C for 4 min and then in a vacuum oven at 10 mT and 250 °C for 1 h). The 600 nm thick layer of Cu was deposited by electron beam evaporation onto the cured PI. Photolithography (AZ Electronic Materials, AZ5214E) and etching (Transene Company, type CE-100 copper etchant at room temperature for 10 s) defined patterns in the metal. After removing the residual photoresist with acetone, spin coating formed another layer of PI on top of the entire structure. Next, photolithography (AZ Electronic Materials, AZ 4620, 2000 rpm for 30 s, baked at 110 for 4 min) and oxygen plasma reaction ion etching (300 mT, 20 sccm O₂, 200 W for 10 min) patterned the PI in geometries to match the metal traces, thereby placing the metal between the two PI layers, at the neutral mechanical plane.

Immersion in hot acetone (~60 °C) partially undercut the underlying PMMA layer, thereby allowing the entire structure to be retrieved from the silicon wafer onto the surface of a piece of water soluble tape (3 M, Inc.). Electron beam evaporation of Ti (5 nm)/SiO₂ (50 nm) through a shadow mask formed backside coatings aligned to the square metal islands. Thin (250 μm thick) silicone substrates (Smooth-On, Ecoflex) were prepared by mixing two components in a 1 : 1 weight ratio, spin-coating (300 rpm for 30 s) the resulting material onto a silicon substrate with arrays of trenches (250 μm deep) that match the geometry and layout of the islands in the island-bridge electrode structure, and then curing it (120 min at room temperature). The as-fabricated silicone substrate with a post array was then activated by exposure to ultraviolet induced ozone for 5 min. Laminating the electrode structures onto the silicone substrate led to strong irreversible bonding upon contact in a way that every island was bonded onto a post and the bridge interconnects were freely suspended between the posts. The water soluble tape was removed by placing the substrate under running tap water for about 1 hour. Mechanical testing was performed with customized uniaxial and biaxial stretchers. Images of the deformed interconnects were collected with a digital single-lens reflex camera.

3 Results and discussion

A schematic illustration of a generic island-bridge structure with serpentine interconnects is shown in Fig. 1a, where periodically distributed posts are adopted to allow freely suspended serpentine interconnects. Optical images and schematic illustrations of the geometry of an individual serpentine interconnect are shown in Fig. 1b and c. A representative unit cell consists of two half circles and two straight lines with the length l_2 and spacing l_1 (Fig. 1c). The number of unit cells in each serpentine interconnect is m . The cross-section has the width w and thickness t . As shown in the following, these parameters affect mechanical deformation *via* three non-dimensional parameters, namely the length/spacing ratio $\alpha = l_2/l_1$, number m of unit cells, and cross-sectional aspect ratio t/w . The following subsections present detailed analysis of the effects of these geometric parameters on buckling behaviors, and further demonstrate an optimized design. The active devices are much stiffer than the buckled interconnects, and therefore their

deformation has a negligible effect on buckling of interconnects,^{27,29,33} as in the following.

3.1 Onset of buckling

The serpentine interconnect spans the space between two rigid device islands (*e.g.*, in Fig. 1a), corresponding to clamped boundary conditions at the two ends. Upon stretching of the entire structure, the serpentine is pulled from the two ends, such that each straight wire and the arc wire segment undergoes combined shearing and bending. As the applied strain reaches a critical value, lateral buckling (or shear buckling) occurs to reduce the strain energy.^{34,40} Similar to Euler buckling, the critical buckling load (P_{cr}) in the case of lateral buckling can be expressed in the form of $P_{cr} = \sqrt{EI_1 GJ_T}/(C_1 L)^2$,³⁴ where L is a length scale of the structure, C_1 is a constant that depends on the boundary conditions, and the torsion stiffness $GJ_T (= wt^3/3)$ and out-of-plane bending stiffness $EI_1 (= wt^3/12)$ are much smaller than the in-plane stiffness ($EI_3 = w^3t/12$) when the cross-section is small (*e.g.*, $t/w < 1/2$). For a serpentine interconnect with two length parameters, l_1 and l_2 , the critical buckling load is given by

$$P_{cr} = \frac{wt^3 \sqrt{EG}}{f_1(m)l_1^2 + f_2(m)l_1l_2 + f_3(m)l_2^2}, \quad (1)$$

where f_1 , f_2 and f_3 describe the contributions of each second-order term of length scale to the lateral buckling. These quantities, which depend only on the number (m) of unit cells in the serpentine, are given in Table S1 (see ESI for details†). The critical buckling strain for the entire structure can be obtained analytically as (see ESI and Fig. S1 for details†)

$$\varepsilon_{cr} = \frac{P_{cr}l_1^2}{48EI_3} \left[4\alpha(\alpha^2 + 6) + 3\pi(2\alpha^2 + 1) - \frac{36(\alpha^2 + \pi\alpha + 2)^2}{8\alpha + \pi + 8(2\alpha + \pi)m^2} \right], \quad (2)$$

where $EI_3 = w^3t/12$ is the in-plane bending stiffness. Substitution of eqn (1) into eqn (2) shows that the critical buckling strain is linearly proportional to the square of the aspect ratio, t^2/w^2 , and is given by

$$\varepsilon_{cr} = \frac{\alpha(\alpha^2 + 6) + \frac{3\pi}{4}(2\alpha^2 + 1) - \frac{9(\alpha^2 + \pi\alpha + 2)^2}{8\alpha + \pi + 8(2\alpha + \pi)m^2}}{f_1(m) + f_2(m)\alpha + f_3(m)\alpha^2} \sqrt{\frac{G}{E}} \frac{t^2}{w^2}. \quad (3)$$

FEM results validate this scaling law for a wide range of aspect ratios α and t/w , as shown in Fig. 2, where the interconnect is made of single-layer gold in the simulations. Eqn (3) shows that the critical strain is linearly proportional to $(t/w)^2$, which is consistent with the numerical results of Fig. 2a, for different combinations $(m, \alpha) = (1, 3)$, $(1, 1)$ and $(2, 3)$ and thin serpentes (*e.g.*, $t/w < 1/2$). Fig. 2b and c illustrate the dependence of the critical buckling strain on the length/spacing ratio and number of unit cells, with reasonable agreement between the analytical and numerical (FEM) results. For one unit cell ($m = 1$), there are two buckling modes, namely “symmetric” and

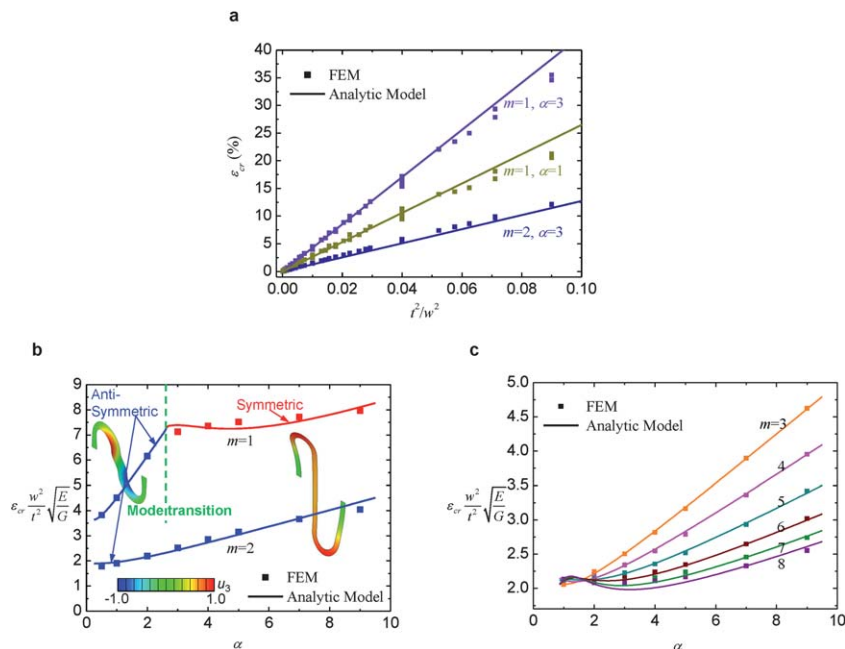


Fig. 2 Critical buckling strain of a serpentine interconnect under stretching, obtained from the analytic model and finite element method. The dependences of critical buckling strain on the square of the cross-sectional aspect ratio (t^2/w^2) for $(m, \alpha) = (1, 1), (1, 3)$ and $(2, 3)$ (a), and the length/spacing ratio (α) for different numbers of unit cells (b and c). The insets of (b) (the deformed serpentine interconnects) show the contour of out-of-plane displacement normalized by its maximum value.

“anti-symmetric” (to be illustrated in detail in Fig. 3). Only the “anti-symmetric” mode occurs for $m > 1$. For the length/spacing ratio $\alpha > 3$, the critical buckling strain for a serpentine with multiple unit cells ($m > 1$) increases linearly with α .

The critical buckling mode determines the subsequent deformation paths in the postbuckling regime. Numerical results by FEM indicate that the critical buckling mode depends mainly on the length/spacing ratio α and number of unit cells m , and is almost independent of the cross-sectional aspect ratio t/w for thin wires (e.g., $t/w < 1/2$) of current interest. Fig. 3a shows a diagram of the critical buckling mode in terms of the length/spacing ratio and number of unit cells. Only the lowest order buckling modes (i.e. those with minimum strain energy) are presented. This diagram illustrates the existence of symmetric and anti-symmetric buckling modes. The symmetric mode can occur when the serpentine interconnect has one unit cell ($m = 1$) and length/spacing ratio $\alpha > 2.4$, while the anti-symmetric mode can occur in all the other cases. Fig. 3b provides diagrams of buckling modes for various m and α , with contours of the normalized out-of-plane displacement u_3 (normalized by the maximum u_3). For $m = 1$, the symmetric mode (the top left corner of Fig. 3b) involves vertical displacement of the entire structure, and u_3 is symmetric about the center. The straight regions on the left and right (attached to two clamped ends) are bent (color changes from green to red), while the straight region in the middle undergoes a rigid body translation (uniformly red color). The strain energy here results mainly from bending and is linearly proportional to $1/L^3$ for displacement loading,⁴⁰ where L is the length. For the anti-symmetric buckling mode with $m = 1$ (e.g., the bottom left corner of Fig. 3b), the two curved parts move vertically up and down, respectively, and u_3 is anti-symmetric

about the center; the straight regions on the left and right have negligible u_3 (uniformly green color); the straight region in the middle undergoes significant twisting, as evidenced by the color change across the width. The strain energy here results mainly from twisting and is linearly proportional to $1/L$.⁴⁰ Comparison of bending energy ($\sim 1/L^3$) to twisting energy ($\sim 1/L$) suggests that the anti-symmetric buckling mode is energetically favorable for short interconnects (i.e., small α). Such mechanisms are confirmed by the critical buckling strains extracted from FEM and their dependence on the length/spacing ratio, as shown in Fig. S2.†

3.2 Postbuckling process and stretchability

As the applied strain exceeds the critical buckling strain, the serpentine structures undergo lateral buckling to reduce the strain energy, and accordingly, the strain level in the structure. This section examines postbuckling behaviors associated with the two modes in Section 3.1, and identifies a scaling law for limits in stretchability.

Fig. 4 illustrates the evolution of deformations associated with the two different buckling modes for strains between 0% and 80%, through experimental images and numerical results. Test samples fabricated for this purpose consist of free-standing, multilayer traces, with materials and stack designs [PI (1.2 μm)/Cu (0.6 μm)/PI (1.2 μm), where PI denotes polyimide], between square pads that bond to raised posts molded onto the surface of an underlying elastomer substrate. Here, the geometric parameters of the serpentes place them in the transition region between two different buckling modes, such that both modes can occur. For the two modes, the left and right wires both experience combined deformations of bending and

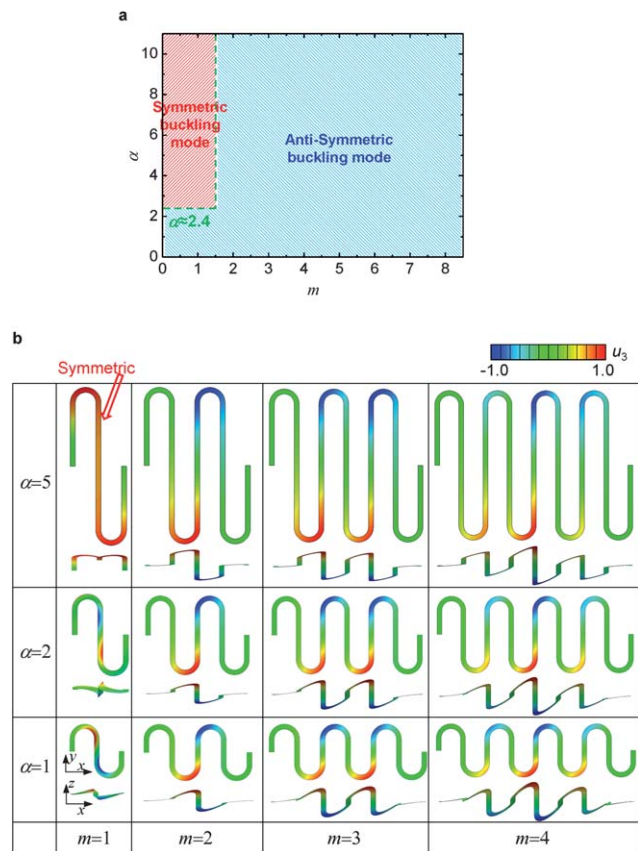


Fig. 3 Experimental and numerical analyses on the buckling mode of the serpentine interconnect under stretching. (a) The buckling modes for various interconnect length/spacing ratios and numbers of unit cells obtained using the finite element method; (b) the distribution of out-of-plane displacement for the buckling modes of the serpentine interconnect with different length/spacing ratios and different numbers of unit cells, based on the finite element method.

twisting during the postbuckling processes. As a consequence, the configurations appear similar in the top view. Nevertheless, the middle regions undergo different deformations: for the symmetric mode, relatively small deformations occur, such that the appearance is flat when viewed from the top; for the anti-symmetric mode, the corresponding region is subject to twisting such that this same region appears to become narrower when viewed from the top with the increase in stretching. Although the deformation processes are completely different for these two modes, variations of the maximum principal strain in the metal layer are similar, as shown in Fig. 4a and c. For a fracture strain (*i.e.*, elongation at break) of 10.0% for copper,⁴¹ numerical results predict a stretchability of $\sim 81\%$ for both buckling modes, which is in reasonable agreement with the experimental measurement (85–90%). For reversible deformation, defined by the condition in which the serpentine interconnect returns to its initial configuration after the applied strain is released, the strain in the metal must remain below the yield strain ($\sim 0.3\%$, for copper).⁴² Here, FEM gives a maximum applied strain of $\sim 43\%$, which again agrees with experimental results (40–50%).

In the following, we analyze the effects of geometric parameters on the maximum strain in the interconnect, and

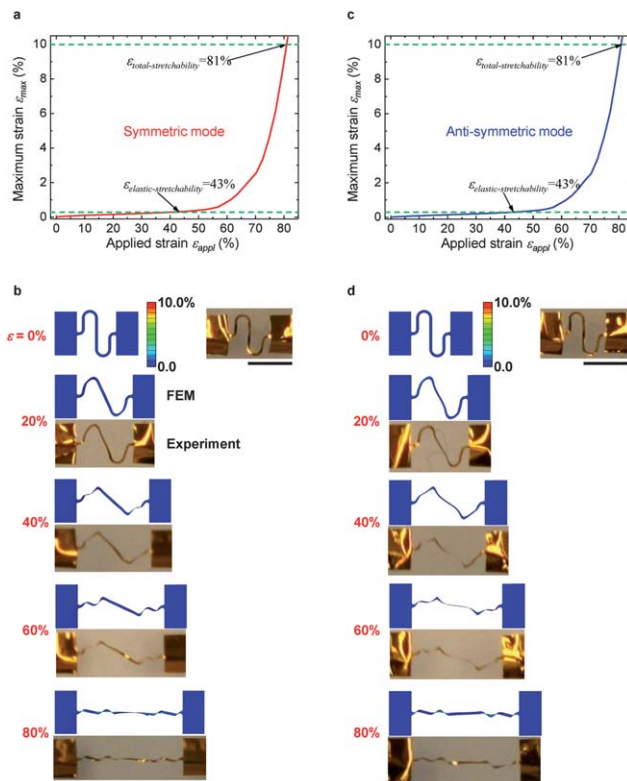


Fig. 4 Experiments and numerical analyses on the buckling mechanisms of the serpentine interconnect with strain from 0% to 80%. The maximum principal strain in the metal layer *versus* the applied strain, and the deformation modes from experiments and numerical analyses, for both the symmetric (a and b) and anti-symmetric (c and d) modes, respectively. The interconnect has $m = 1$ unit cell, length/spacing ratio $\alpha = 2.4$, cross-sectional aspect ratio $t/w = 0.1$, and normalized spacing $l_1/w = 10$. The scale bars in (b) and (d) are 1 mm.

determine a scaling law for elastic stretchability (the maximum applied strain for reversible deformation) of the whole structure. The out-of-plane and in-plane bending strains during the lateral postbuckling processes are proportional to the thickness and width, respectively.³⁴ For the serpentine structure, the maximum principal strain during reversible deformation in the postbuckling regime can be expressed as

$$\epsilon_{\max} = F_1(\epsilon_{\text{appl}}, m, \alpha) \frac{t}{l_1} + F_2(\epsilon_{\text{appl}}, m, \alpha) \frac{w}{l_1}, \quad (4)$$

where F_1 and F_2 are non-dimensional functions of the applied strain ϵ_{appl} , m is the number of unit cells, and α is the length/spacing ratio. Such a linear dependence on the cross-sectional thickness and width is well supported by FEM for various loading stages, as shown in Fig. S3.† The out-of-plane bending strain is linearly proportional to the square root of the applied strain during postbuckling,³⁴ *i.e.*, $F_1 \sim \sqrt{\epsilon_{\text{appl}}}$, which is confirmed by FEM as shown in Fig. S4.† The numerical results in Fig. S4† also show that the function F_2 is linearly proportional to the square of the applied strain, ϵ_{appl}^2 , such that eqn (4) can be written as

$$\epsilon_{\max} = g_1(m, \alpha) \sqrt{\epsilon_{\text{appl}}} \frac{t}{l_1} + g_2(m, \alpha) \epsilon_{\text{appl}}^2 \frac{w}{l_1}, \quad (5)$$

where g_1 and g_2 are the coefficients of proportionality between F_1 and $\sqrt{\epsilon_{\text{appl}}}$ and between F_2 and ϵ_{appl}^2 , respectively, and both

depend on the number of unit cells m and the length/spacing ratio α , and are given in Tables S2 and S3 (see ESI for details[†]); with the increase of α , both g_1 and g_2 decrease and become independent of m , for $m \geq 6$. The out-of-plane bending strain [the first term on the right hand side of eqn (5)] dominates in the initial stage of postbuckling, where the applied strain is small (such that $\sqrt{\varepsilon_{\text{appl}}} \gg \varepsilon_{\text{appl}}^2$). The in-plane bending strain [the second term on the right hand side of eqn (5)] takes effect only when the applied strain is relatively large ($\sqrt{\varepsilon_{\text{appl}}} \sim \varepsilon_{\text{appl}}^2$). Based on eqn (5) and the yield criterion of $\varepsilon_{\text{max}} = \varepsilon_{\text{yield}}$, where $\varepsilon_{\text{yield}}$ is the yield strain of the interconnect material (e.g., 0.3% for copper), the elastic stretchability of the serpentine can be written as

$$\varepsilon_{\text{elastic-stretchability}} = \lambda^2, \quad (6)$$

where $\lambda > 0$ is the solution of the following 4th order algebraic equation that has a single positive solution,

$$g_2(m, \alpha)\lambda^4 + g_1(m, \alpha)\lambda - \frac{\varepsilon_{\text{yield}}l_1}{w} = 0. \quad (7)$$

Eqn (6) and (7) indicate that the elastic stretchability increases with decreasing serpentine thickness (*via* t/w) or increasing spacing or yield strain (*via* $\varepsilon_{\text{yield}}l_1/w$). These predictions agree well with the numerical results for a large range of t/w and $\varepsilon_{\text{yield}}l_1/w$, as demonstrated in Fig. 5a for $m = 1$ and $\alpha = 3$. Here, the interconnect is made of single-layer gold in the simulations, in order to be consistent with the theory. The thickness, width, spacing and yield strain come into play *via* two dimensionless combinations, namely t/w and $\varepsilon_{\text{yield}}l_1/w$. Fig. 5b shows the effects of the other two non-dimensional parameters, namely the number of unit cells m and the length/spacing ratio α , for $t/w = 0.05$ and $\varepsilon_{\text{yield}}l_1/w = 0.015$. The elastic stretchability increases with increasing length/spacing ratio, and is essentially independent of m for $m \geq 6$. In practical applications, the physical space for the serpentine is limited. This situation often demands large numbers of unit cells to achieve large length/spacing ratios (and thus large stretchability), in layouts that maintain a relatively small amplitude.

Eqn (6) and (7) define the limits for elastic behavior in the serpentine; below these limits, the structure returns to its initial

configuration after release of the applied strain. Irreversible, plastic deformation occurs once the applied strain exceeds the elastic limit. To explore this regime, we adopt an elastic-ideally plastic constitutive model⁴³ for the metal layer (e.g., copper in experiments) to calculate the total stretchability, as defined by the applied strain required to induce ε_{max} that reaches the failure strain $\varepsilon_{\text{failure}}$. Fig. 4 demonstrates that both the predicted total stretchability (81%) and interconnect deformation beyond the elastic stretchability (43%) agree well with the experimental results ($85\% < \varepsilon_{\text{total-stretchability}} < 90\%$, $40\% < \varepsilon_{\text{elastic-stretchability}} < 50\%$, and optical images). It should be pointed out that the elastic-ideally plastic model neglects plastic work hardening and therefore underestimates the total stretchability. The above analyses suggest that the elastic and full stretchabilities increase as the metal layer decreases. For example, the widely used bilayer of 5 nm Cr and 100 nm Au would give larger stretchability than the 600 nm Cu.

3.3 Application of serpentine interconnects in the island-bridge structure

The above analysis can be used to guide designs of the island-serpentine bridge structure (Fig. 1) that achieve simultaneously high areal coverage of the active device and large elastic reversibility of the entire system. For square islands,^{15,16,26} a high areal coverage requires spacing between neighboring islands that are small compared to their characteristic sizes. By contrast, large elastic stretchability demands large spacing so as to accommodate long interconnects. To balance these two competing goals, previous designs exploited surface relief structures on the elastomer substrates with buckled interconnects (originally straight and then buckled, *via* use of pre-strain in the substrate).^{26,35} This approach is useful, but practically limited, in most cases, to levels of total stretchability less than 50%, without sacrificing areal coverage, mainly due to the relatively short interconnects and their inability to make efficient use of the space between the islands. Serpentine interconnects resolve this issue by providing a space-filling curvature that maximizes utilization of this area.

Fig. 6 demonstrates a stretchable copper electrode with a serpentine interconnect (see Fig. S5 for detailed dimensions[†]) and square posts (with a depth of 250 μm) between the substrate

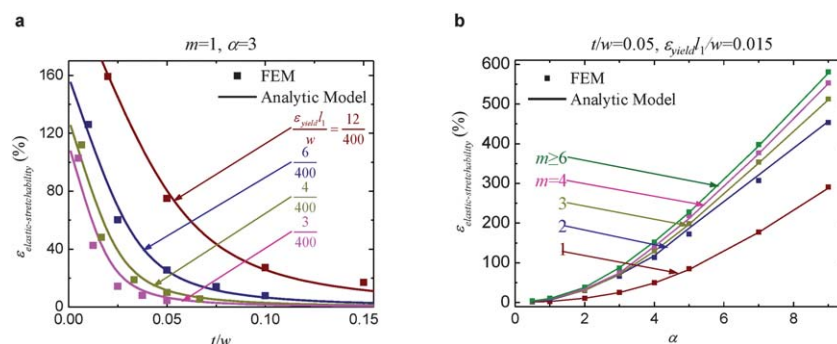


Fig. 5 The scaling law of elastic stretchability. (a) The elastic stretchability *versus* the cross-sectional aspect ratio t/w for various $\varepsilon_{\text{yield}}l_1/w$, $m = 1$ and $\alpha = 3$; (b) the elastic stretchability *versus* the length/spacing ratio α of the interconnect for various unit cell numbers m , $t/w = 0.05$, and $\varepsilon_{\text{yield}}l_1/w = 0.015$.

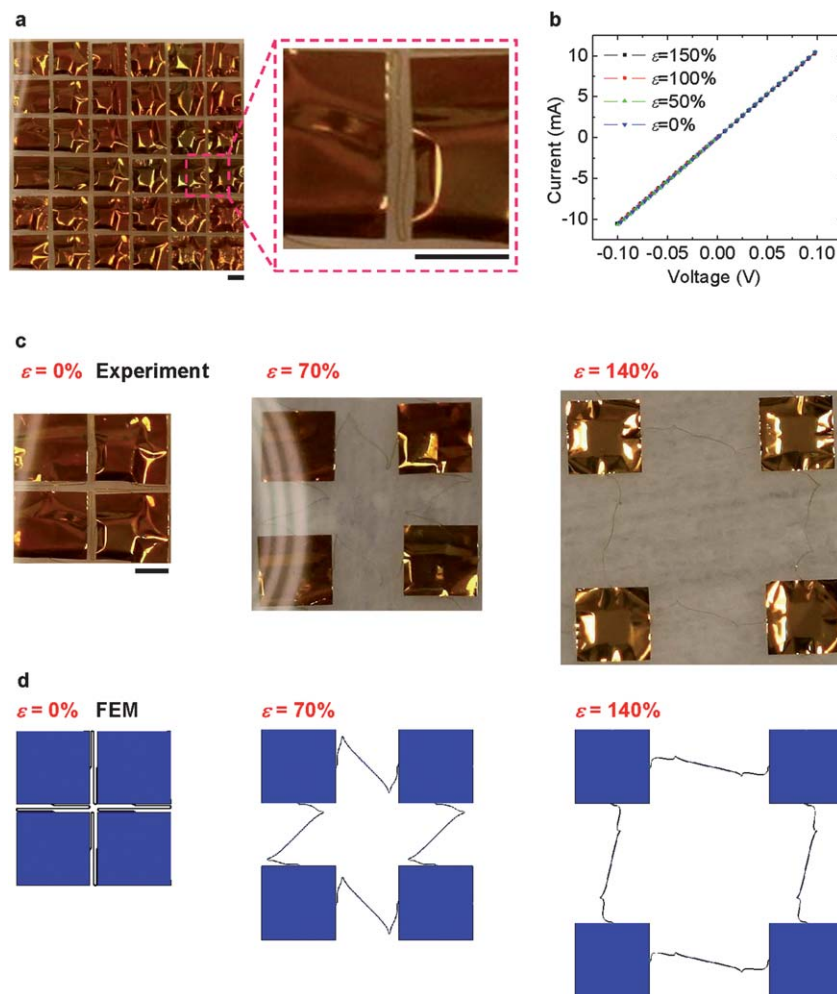


Fig. 6 Design optimization of the serpentine interconnect for the island-bridge structure with ultra-high areal coverage ($\sim 81\%$) and total stretchability ($\sim 172\%$). (a) Optical images of the island-bridge structure with a 6×6 array; (b) the I - V curves of the serpentine interconnects under different levels of biaxial strains (0%, 50%, 100% and 150%), indicating the minimum effect of the strain on the interconnect conductivity; (c) experimental and (d) numerical results of the deformation modes under different levels of biaxial strains (ϵ). The scale bars in (a) and (c) are 1 mm.

and islands, which, as confirmed by experiments and numerical simulations, has an areal coverage of 81%, and a biaxial elastic stretchability of 134% and total stretchability of 172%. Test samples fabricated for this purpose consist of a free-standing copper interconnect ($0.6 \mu\text{m}$ in thickness) sandwiched by two PI layers ($1.2 \mu\text{m}$ in thickness). Besides the utilization of square posts (Fig. S6b[†]), the technique of selective bonding (Fig. S6a[†]) could also be adopted to avoid a drastic strain concentration in the substrate. The predicted deformation modes (in Fig. 6d) by FEM show reasonable agreement with the optical images (in Fig. 6c). In the experiment, the interconnect fractures when the biaxial applied strain is between $\sim 150\%$ and $\sim 180\%$, which agrees well with predictions from FEM ($\sim 172\%$). Even up to biaxial strains of $\sim 150\%$, the electrical resistances of the serpentine interconnects, as measured between two adjacent islands, are similar to values in the undeformed state, as seen in the measured current-voltage curves of Fig. 6b. Although the copper interconnects have piezoresistance (with a gauge factor of ~ 2),⁴⁴ the resistance essentially does not change even under

extreme stretching (e.g., $\sim 150\%$) because of the low strain level in the interconnect ($< 0.51\%$ for 150% biaxial stretching) and the localized characteristics of strain distribution shown in Fig. 4. Serpentes with these geometries can be nearly fully extended before failure. The areal coverage and stretchability both exceed values achieved in recently reported examples that use straight, Euler buckled interconnects.^{26,35}

4 Conclusion

The work presented here represents systematic studies of critical buckling strains and postbuckling behaviors of serpentine structures suitable as interconnects in stretchable electronics, through analytical modeling, FEM, and experiments. The resulting scaling laws can be useful in the development of future designs. Both numerical and experimental results show two (symmetric and anti-symmetric) buckling modes and the parameters, *i.e.* the length/spacing ratio and the number of unit cells, that govern their occurrence. The detailed deformations

for both modes and their dependence on applied strain are revealed through numerical simulations and experimental images. The collective results allow straightforward optimization in the design of island-bridge structures to balance areal coverage of the islands with stretchability. The enhancement of system stretchability (*e.g.*, to >150%) in the design of an island-bridge structure also requires the development of high-performance soft materials, or novel structural design in the soft substrate, such as fabricating surface relief structures as presented herein. This is because without using these relief structures, the substrate between two neighboring islands would experience extremely large strain (*e.g.*, ~1000%, larger than the fracture strain of most soft materials) for a large areal coverage (*e.g.*, ~81%) and applied strain (*e.g.*, ~100%). The concepts presented have general utility for future work in stretchable semiconductor systems, especially those that demand high coverage of active devices, such as stretchable energy storage devices,⁴⁵ photovoltaics,⁴³ and electronic eye-ball cameras.¹⁵

Acknowledgements

Y. H. and J. A. R. acknowledge the support from NSF (ECCS-0824129 and CMMI-0749028). Y. H. also acknowledges the support from NSFC.

References

- 1 S. P. Lacour, S. Wagner, Z. Y. Huang and Z. Suo, *Appl. Phys. Lett.*, 2003, **82**, 2404–2406.
- 2 S. P. Lacour, J. Jones, S. Wagner, T. Li and Z. G. Suo, *Proc. IEEE*, 2005, **93**, 1459–1467.
- 3 D. Y. Khang, H. Q. Jiang, Y. Huang and J. A. Rogers, *Science*, 2006, **311**, 208–212.
- 4 T. Sekitani, Y. Noguchi, K. Hata, T. Fukushima, T. Aida and T. Someya, *Science*, 2008, **321**, 1468–1472.
- 5 T. Sekitani, H. Nakajima, H. Maeda, T. Fukushima, T. Aida, K. Hata and T. Someya, *Nat. Mater.*, 2009, **8**, 494–499.
- 6 M. Kaltenbrunner, G. Kettlgruber, C. Siket, R. Schwodiauer and S. Bauer, *Adv. Mater.*, 2010, **22**, 2065–2067.
- 7 J. A. Rogers, T. Someya and Y. G. Huang, *Science*, 2010, **327**, 1603–1607.
- 8 Z. G. Suo, *MRS Bull.*, 2012, **37**, 218–225.
- 9 S. Wagner and S. Bauer, *MRS Bull.*, 2012, **37**, 207–217.
- 10 T. Sekitani and T. Someya, *MRS Bull.*, 2012, **37**, 236–245.
- 11 P. Gorrn, W. Z. Cao and S. Wagner, *Soft Matter*, 2011, **7**, 7177–7180.
- 12 Y. Hwang, H. A. Cho, S. H. Kim, H. S. Jang, Y. Hyun, J. Y. Chun, S. J. Park and H. C. Ko, *Soft Matter*, 2012, **8**, 7598–7603.
- 13 J. Yoon, A. J. Baca, S. I. Park, P. Elvikis, J. B. Geddes, L. F. Li, R. H. Kim, J. L. Xiao, S. D. Wang, T. H. Kim, M. J. Motala, B. Y. Ahn, E. B. Duoss, J. A. Lewis, R. G. Nuzzo, P. M. Ferreira, Y. G. Huang, A. Rockett and J. A. Rogers, *Nat. Mater.*, 2008, **7**, 907–915.
- 14 D. H. Kim, N. S. Lu, R. Ma, Y. S. Kim, R. H. Kim, S. D. Wang, J. Wu, S. M. Won, H. Tao, A. Islam, K. J. Yu, T. I. Kim, R. Chowdhury, M. Ying, L. Z. Xu, M. Li, H. J. Chung, H. Keum, M. McCormick, P. Liu, Y. W. Zhang, F. G. Omenetto, Y. G. Huang, T. Coleman and J. A. Rogers, *Science*, 2011, **333**, 838–843.
- 15 H. C. Ko, M. P. Stoykovich, J. Z. Song, V. Malyarchuk, W. M. Choi, C. J. Yu, J. B. Geddes, J. L. Xiao, S. D. Wang, Y. G. Huang and J. A. Rogers, *Nature*, 2008, **454**, 748–753.
- 16 G. Shin, I. Jung, V. Malyarchuk, J. Z. Song, S. D. Wang, H. C. Ko, Y. G. Huang, J. S. Ha and J. A. Rogers, *Small*, 2010, **6**, 851–856.
- 17 B. P. Timko, T. Cohen-Karni, G. H. Yu, Q. Qing, B. Z. Tian and C. M. Lieber, *Nano Lett.*, 2009, **9**, 914–918.
- 18 J. Viventi, D. H. Kim, J. D. Moss, Y. S. Kim, J. A. Blanco, N. Annetta, A. Hicks, J. L. Xiao, Y. G. Huang, D. J. Callans, J. A. Rogers and B. Litt, *Sci. Transl. Med.*, 2010, **2**, 24ra22.
- 19 S. Wagner, S. P. Lacour, J. Jones, P. H. I. Hsu, J. C. Sturm, T. Li and Z. G. Suo, *Phys. E*, 2004, **25**, 326–334.
- 20 T. Someya, T. Sekitani, S. Iba, Y. Kato, H. Kawaguchi and T. Sakurai, *Proc. Natl. Acad. Sci. U. S. A.*, 2004, **101**, 9966–9970.
- 21 S. C. B. Mannsfeld, B. C. K. Tee, R. M. Stoltenberg, C. Chen, S. Barman, B. V. O. Muir, A. N. Sokolov, C. Reese and Z. N. Bao, *Nat. Mater.*, 2010, **9**, 859–864.
- 22 K. Takei, T. Takahashi, J. C. Ho, H. Ko, A. G. Gillies, P. W. Leu, R. S. Fearing and A. Javey, *Nat. Mater.*, 2010, **9**, 821–826.
- 23 T. Sekitani and T. Someya, *Adv. Mater.*, 2010, **22**, 2228–2246.
- 24 T. Sekitani, U. Zschieschang, H. Klauk and T. Someya, *Nat. Mater.*, 2010, **9**, 1015–1022.
- 25 D. H. Kim, N. S. Lu, Y. G. Huang and J. A. Rogers, *MRS Bull.*, 2012, **37**, 226–235.
- 26 J. Lee, J. A. Wu, M. X. Shi, J. Yoon, S. I. Park, M. Li, Z. J. Liu, Y. G. Huang and J. A. Rogers, *Adv. Mater.*, 2011, **23**, 986–991.
- 27 D. H. Kim, J. Z. Song, W. M. Choi, H. S. Kim, R. H. Kim, Z. J. Liu, Y. Y. Huang, K. C. Hwang, Y. W. Zhang and J. A. Rogers, *Proc. Natl. Acad. Sci. U. S. A.*, 2008, **105**, 18675–18680.
- 28 D. H. Kim, Y. S. Kim, J. Wu, Z. J. Liu, J. Z. Song, H. S. Kim, Y. G. Y. Huang, K. C. Hwang and J. A. Rogers, *Adv. Mater.*, 2009, **21**, 3703–3707.
- 29 D. H. Kim, Z. J. Liu, Y. S. Kim, J. Wu, J. Z. Song, H. S. Kim, Y. G. Huang, K. C. Hwang, Y. W. Zhang and J. A. Rogers, *Small*, 2009, **5**, 2841–2847.
- 30 R. H. Kim, H. Tao, T. I. Kim, Y. H. Zhang, S. Kim, B. Panilaitis, M. M. Yang, D. H. Kim, Y. H. Jung, B. H. Kim, Y. H. Li, Y. G. Huang, F. G. Omenetto and J. A. Rogers, *Small*, 2012, **8**, 2812–2818.
- 31 T. Li, Z. G. Suo, S. P. Lacour and S. Wagner, *J. Mater. Res.*, 2005, **20**, 3274–3277.
- 32 H. Q. Jiang, Y. G. Sun, J. A. Rogers and Y. G. Huang, *Int. J. Solids Struct.*, 2008, **45**, 2014–2023.
- 33 J. Song, Y. Huang, J. Xiao, S. Wang, K. C. Hwang, H. C. Ko, D. H. Kim, M. P. Stoykovich and J. A. Rogers, *J. Appl. Phys.*, 2009, **105**, 123516.
- 34 Y. W. Su, J. Wu, Z. C. Fan, K. C. Hwang, J. Z. Song, Y. G. Huang and J. A. Rogers, *J. Mech. Phys. Solids*, 2012, **60**, 487–508.

- 35 J. Lee, J. Wu, J. H. Ryu, Z. J. Liu, M. Meitl, Y. W. Zhang, Y. G. Huang and J. A. Rogers, *Small*, 2012, **8**, 1851–1856.
- 36 Y. G. Sun, W. M. Choi, H. Q. Jiang, Y. G. Y. Huang and J. A. Rogers, *Nat. Nanotechnol.*, 2006, **1**, 201–207.
- 37 M. Gonzalez, F. Axisa, F. Bossuyt, Y. Y. Hsu, B. Vandeveldel and J. Vanfleteren, *Circuit World*, 2009, **35**, 22–29.
- 38 M. Gonzalez, F. Axisa, M. V. BuIcke, D. Brosteaux, B. Vandeveldel and J. Vanfleteren, *Microelectron. Reliab.*, 2008, **48**, 825–832.
- 39 O. van der Sluis, Y. Y. Hsu, P. H. M. Timmermans, M. Gonzalez and J. P. M. Hoefnagels, *J. Phys. D: Appl. Phys.*, 2011, **44**, 034008.
- 40 S. Timoshenko and J. Gere, *Theory of Elastic Stability*, McGraw-Hill, New York, 1961.
- 41 J. R. Davis, *Asm Specialty Handbook: Copper and Copper Alloys*, ASM International, United States of America, 2001.
- 42 F. R. William, D. S. Leroy and H. M. Don, *Mechanics of Materials*, Jon Wiley & Sons, New York, 1999.
- 43 R. Hill, *The Mathematical Theory of Plasticity*, Oxford University Press, New York, 1950.
- 44 S. U. Jen, C. C. Yu, C. H. Liu and G. Y. Lee, *Thin Solid Films*, 2003, **434**, 316–322.
- 45 S. Xu, Y. H. Zhang, J. Cho, J. Lee, X. Huang, L. Jia, J. A. Fan, Y. W. Su, J. Su, H. G. Zhang, H. Y. Cheng, B. W. Lu, C. J. Yu, C. Chuang, T. I. Kim, T. Song, K. Shigeta, S. Kang, C. Dagdeviren, I. Petrov, P. V. Braun, Y. Huang, U. Paik and J. A. Rogers, *Nat. Commun.*, 2013, **4**, 1543.